Article

Kainate receptor modulation by NETO2

https://doi.org/10.1038/s41586-021-03936-y

Received: 12 May 2021

Accepted: 20 August 2021

Published online: 22 September 2021

Check for updates

Lingli He[1,2,3,8], Jiahui Sun[4,5,8], Yiwei Gao[1,3,8], Bin Li[1,3], Yuhang Wang[1,3], Yanli Dong[1,2,3], Weidong An[1,3], Hang Li[1,3], Bei Yang[1,2,3], Yuhan Ge[4,5], Xuejun Cai Zhang[1,3]✉, Yun Stone Shi[4,5,6,7]✉ & Yan Zhao[1,2,3]✉

Glutamate-gated kainate receptors are ubiquitous in the central nervous system of vertebrates, mediate synaptic transmission at the postsynapse and modulate transmitter release at the presynapse[1–7]. In the brain, the trafficking, gating kinetics and pharmacology of kainate receptors are tightly regulated by neuropilin and tolloid-like (NETO) proteins[8–11]. Here we report cryo-electron microscopy structures of homotetrameric GluK2 in complex with NETO2 at inhibited and desensitized states, illustrating variable stoichiometry of GluK2–NETO2 complexes, with one or two NETO2 subunits associating with GluK2. We find that NETO2 accesses only two broad faces of kainate receptors, intermolecularly crosslinking the lower lobe of $ATD^{A/C}$, the upper lobe of $LBD^{B/D}$ and the lower lobe of $LBD^{A/C}$, illustrating how NETO2 regulates receptor-gating kinetics. The transmembrane helix of NETO2 is positioned proximal to the selectivity filter and competes with the amphiphilic H1 helix after M4 for interaction with an intracellular cap domain formed by the M1–M2 linkers of the receptor, revealing how rectification is regulated by NETO2.

Kainate receptors (KARs) are a class of ionotropic glutamate receptors, activated by the neurotransmitter glutamate[1–3]. They are not only located at the postsynapse to mediate excitatory neurotransmission in many brain regions[4,5] but also appear at the presynapse to modulate transmitter release on both excitatory and inhibitory synapses[6,7]. NETO proteins are single-pass transmembrane proteins with an extracellular domain containing two C1r/C1s–Uegf–BMP domains (known as CUB1 and CUB2) and a low-density lipoprotein class A domain (LDLa). These proteins have been identified as an auxiliary component of native KARs and significantly affect KAR trafficking, gating and pharmacology[8–11]. More specifically, NETO2 modulates KAR gating by slowing deactivation and desensitization, accelerating recovery from desensitization and attenuating polyamine block of calcium-permeable KARs[12,13]. Despite recent progress in the structural study of isolated KARs[14–18], the molecular basis of regulatory roles of NETO proteins remains unclear. Here we show the architectures of the GluK2–NETO2 complex in the antagonist-bound closed state and the agonist-bound desensitized state, illustrating interactions and stoichiometry between GluK2 and NETO2, and the modulation mechanism of NETO2 on GluK2 receptor gating and pore properties. Moreover, a more-complete pore domain, including a detailed structure of the selectivity filter, is provided in our structures.

Cryo-EM analysis of the GluK2–NETO2 complex

To investigate the structural basis for modulation of GluK2 gating by NETO2, we co-expressed both the full-length GluK2 (with Gln at the Q/R site) and NETO2 in HEK 293T cells and purified the complex[19] (Extended Data Fig. 1). Our cryo-electron microscopy (cryo-EM) studies generated three distinct assemblies of the antagonist-bound GluK2–NETO2 complexes, including GluK2 bound with one NETO2 (GluK2-1×NETO2) or two NETO2 (GluK2-2×NETO2) (Fig. 1a, b, Extended Data Fig. 2a). The third type of complex features a disrupted ligand-binding domain (LBD) dimer on one side and an intact LBD dimer on the other side, the latter of which is also bound with one NETO2 subunit, and thus this complex is denoted as GluK2-1×$NETO2^{asymLBD}$ (Fig. 1c, Extended Data Fig. 2a). The GluK2-1×NETO2, GluK2-2×NETO2 and GluK2-1×$NETO2^{asymLBD}$ complexes were determined at 4.2 Å, 6.4 Å and 4.1 Å resolutions (Extended Data Fig. 2b–j), respectively. The LBD–transmembrane domain (TMD) focused classification and refinement of the GluK2-1×NETO2 complex yield a 3.9 Å map with more density features (Extended Data Figs. 2k–m, 3a, b). Detailed data processing and model building are described in the Methods section.

Architectures of the GluK2–NETO2 complex

The overall structure of NETO2 is about 140 Å in height, composed of four domains including CUB1, CUB2, LDLa and TM1 (Fig. 1d). There is a horizontal helix, termed α1, right before TM1 of NETO2 ($TM1^{NETO2}$) (Fig. 1d). The CUB1, CUB2 and LDLa domains are closely packed together. The linker between LDLa and α1 helix was missing, probably due to conformational heterogeneity (Fig. 1d). On the GluK2 side, the model of both the GluK2-1×NETO2 and the GluK2-2×NETO2 complexes reveals that the M3 gate is closed and the degree of LBD clamshell closure is nearly identical to the isolated GluK2 LBD structure bound with LY466195 (Protein Data Bank (PDB) ID: 5KUH), confirming that the complex is stabilized at the antagonist-bound inhibited state (Fig. 1e, Extended Data Fig. 4a). In the case of the GluK2-1×NETO2 complex, the

[1]National Laboratory of Biomacromolecules, CAS Center for Excellence in Biomacromolecules, Institute of Biophysics, Chinese Academy of Sciences, Beijing, China. [2]State Key Laboratory of Brain and Cognitive Science, Institute of Biophysics, Chinese Academy of Sciences, Beijing, China. [3]College of Life Sciences, University of Chinese Academy of Sciences, Beijing, China. [4]Ministry of Education Key Laboratory of Model Animal for Disease Study, Model Animal Research Center, Medical School, Nanjing University, Nanjing, China. [5]State Key Laboratory of Pharmaceutical Biotechnology, Department of Neurology, Affiliated Drum Tower Hospital of Nanjing University Medical School, Nanjing University, Nanjing, China. [6]Institute for Brain Sciences, Nanjing University, Nanjing, China. [7]Chemistry and Biomedicine Innovation Center, Nanjing University, Nanjing, China. [8]These authors contributed equally: Lingli He, Jiahui Sun, Yiwei Gao. ✉e-mail: zhangc@ibp.ac.cn; yunshi@nju.edu.cn; zhaoy@ibp.ac.cn

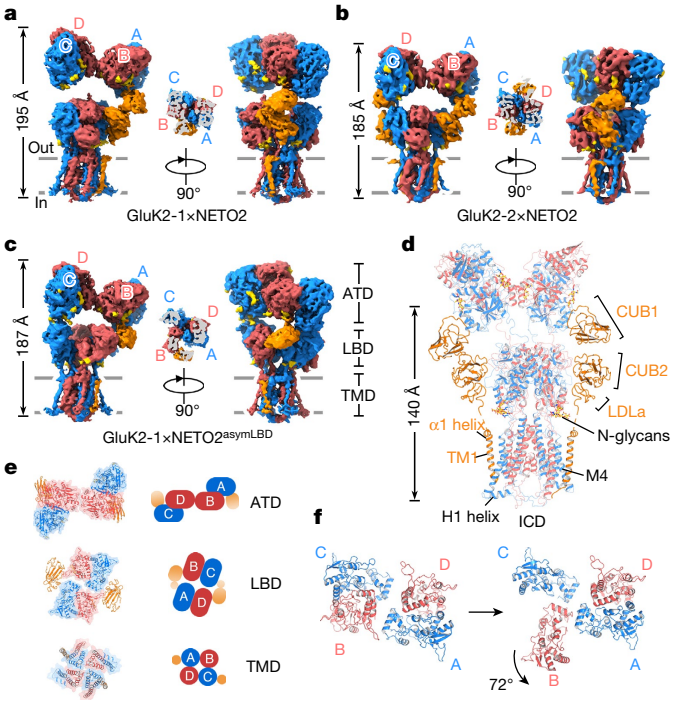

Fig. 1 | Architectures of the GluK2–NETO2 complexes. a–c, Cryo-EM reconstructions of the GluK2-1×NETO2 (**a**), GluK2-2×NETO2 (**b**) and GluK2-1×NETO2^{asymLBD} (**c**) complexes, bound with DNQX. Subunits A/C and B/D of the GluK2 receptor are coloured in blue and red, respectively. NETO2 is coloured in orange. The height of each complex is indicated. Cross-sections of the LBD layer of corresponding complexes are shown in the middle in a smaller scale. **d**, Architecture of the GluK2-2×NETO2 complex. *N*-linked carbohydrates are shown as 'sticks'. ICD, intracellular cap domain. **e**, Top-down view of the ATD–CUB1 layer, the LBD–CUB2–LDLa layer and the TMD–TM1^{NETO2} layer. **f**, Conformational rearrangement of the LBD layer between the GluK2-1×NETO2 complex and the GluK2-1×NETO2^{asymLBD} complex.

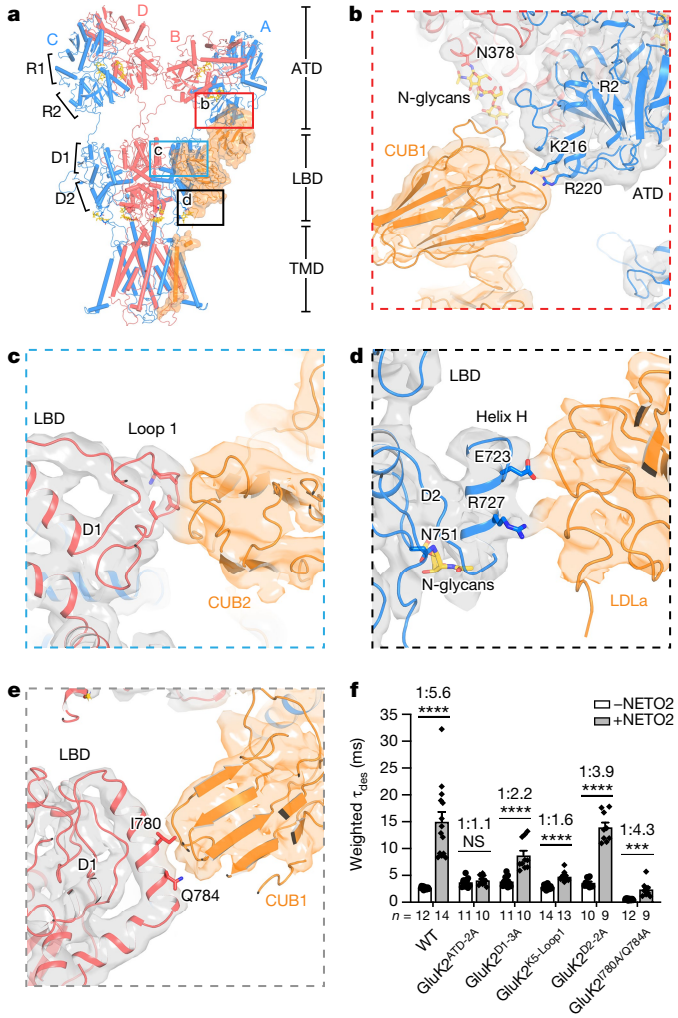

Fig. 2 | Extracellular interactions between GluK2 and NETO2. a, Overall structure of the GluK2-2×NETO2 complex. Subunits A/C and B/D of GluK2 are coloured in blue and red, respectively. NETO2 is shown in a transparent orange surface. **b–d**, Three regions involved in the GluK2–NETO2 interaction are highlighted, including ATD (R2-lobe) with CUB1 (**b**), LBD (D1-lobe) with CUB2 (**c**) and LBD (D2-lobe) with LDLa (**d**). The sidechains of critical residues for GluK2–NETO2 interactions are shown as sticks. The EM map is overlaid on the models of GluK2 and NETO2 as transparent surfaces, coloured in grey (receptor) and orange (NETO2), respectively. **e**, CUB1 and LBD interactions determined in the GluK2-1×NETO2^{asymLBD} complex. **f**, Analysis of the time constant of desensitization of the wild-type (WT) GluK2 and GluK2 mutants, in either the presence or the absence of NETO2. Time constant ratios of recordings with or without NETO2 are indicated. Each symbol represents a single-cell recording, and the *n* value represents independent cells for statistical analysis. Significances were determined using two-sided, unpaired *t*-test. ****$P < 0.0001$; not significant (NS), $P = 0.3959$ (GluK2^{ATD-2A}); ***$P = 0.0002$ (GluK2$^{I780A/Q784A}$). Data are mean ± s.e.m.

distance between the amino-terminal domain (ATD) and LBD layers at the NETO2-bound side is substantially shortened compared with the non-NETO2-bound side, thus breaking from the ideal overall two-fold symmetry of the receptor complex, as evidenced by the ATD–LBD layers from the A and C positions, which are not superimposable with each other (Extended Data Fig. 4b). In addition, the overall structure of the GluK2-2×NETO2 complex also breaks two-fold symmetry (Extended Data Fig. 4b). In particular, the interaction between CUB1 and CUB2 on one side is more extensive than that on the other side.

The GluK2-1×NETO2^{asymLBD} complex contains one disrupted LBD dimer, showing that the LBD of the B subunit rotates approximate 72° relative to that of two-fold-related LBDs (Fig. 1f), which is also consistent with observations from GluK3 structures[16]. One extracellular domain of NETO2 connects ATD with LBD (Fig. 1c). We speculate that this domain is CUB1 as it has a similar binding mode with GluK2 ATD (Extended Data Fig. 4c). Considering that the TM1^{NETO2} helix remains present in the structure, the absence of CUB2 and LDLa in the EM map is probably due to conformational flexibility.

Interactions between GluK2 and NETO2

On the extracellular side of both the GluK2-1×NETO2 and the GluK2-2×NETO2 complexes, the N-terminal CUB1 of NETO2 interacts with the lower lobe in the ATD layer of the A/C subunit of GluK2 (R2-lobe$^{A/C}$). In the LBD layer, the CUB2 and LDLa domains of NETO2 interact with the upper lobe of subunit B/D (D1-lobe$^{B/D}$) and the lower lobe of subunit A/C (D2-lobe$^{A/C}$), respectively (Fig. 2a). This spatial arrangement of GluK2–NETO2 interactions leads to a stoichiometry between GluK2 and NETO2 of either 4:1 or 4:2, which is distinct from the 4:4 stoichiometry between the AMPA receptor and TARPγ2 (ref. [20]). Taking a close look at the GluK2–NETO2 interface, we found that some charged residues from GluK2 contact the extracellular domains of NETO2. For instance, K216/R220 on the ATD layer and E723/R727 on the LBD layer potentially form electrostatic interactions with NETO2 (Fig. 2b, d, Extended Data Fig. 5a, c). Unlike a point-to-point interaction mode, CUB2 forms more extensive interactions with loop 1 (residues 448–453) (Fig. 2c). Although their sequence identity is low (Extended Data Fig. 5b), the loop 1 from different isoforms adopt similar 3D conformations (Extended Data Fig. 5e). In the GluK2-1×NETO2^{asymLBD} complex,

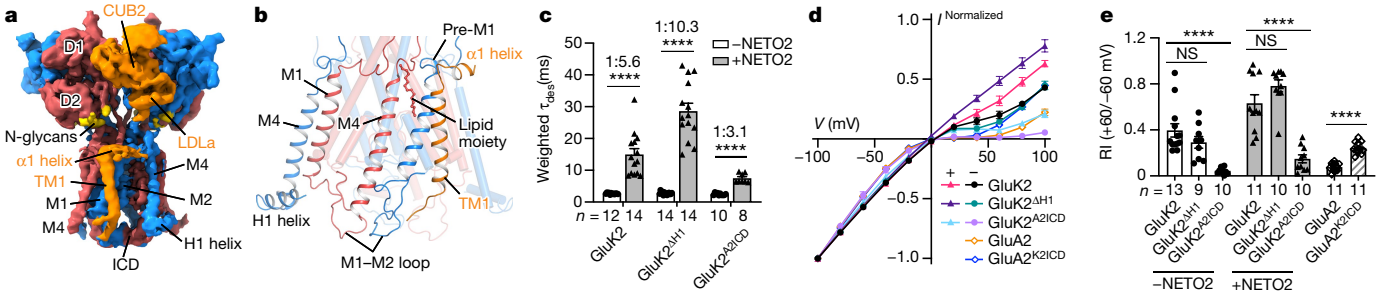

Fig. 3 | Ion conduction pore of GluK2 and the modulation mechanism of inward rectification. a, EM density map of the LBD and TMD layers of the GluK2-1×NETO2 complex. Subunits A/C and B/D of GluK2 are coloured in blue and red, respectively. NETO2 is coloured in orange. N-glycans are coloured in yellow. **b**, The interactions between GluK2 and NETO2 at the TMD and ICD layers. **c**, Quantification of the desensitization time constant of WT GluK2, GluK2$^{\Delta H1}$ and GluK2^{A2ICD}, in the absence or presence of NETO2. Each symbol represents a single recording. Significances were determined using two-sided, unpaired *t*-test. ****$P < 0.0001$. **d**, Normalized current–voltage relationship of GluK2, GluA2 or their mutants. The sample size is as in **e**. **e**, The rectification index (RI) is calculated by dividing the current amplitude at +60 mV by that at −60 mV. Each symbol represents a single recording.The *n* value represents independent cells for statistical analysis. Significances were determined using two-sided, unpaired *t*-test. ****$P < 0.0001$. NS, GluK2 versus GluK2$^{\Delta H1}$, $P = 0.2155$; GluK2 + NETO2 versus GluK2$^{\Delta H1}$ + NETO2, $P = 0.1229$. Data are mean ± s.e.m.

one of the LBD dimers is disrupted (Fig.1f), consequently yielding a new interaction between CUB1 and D1-lobe$^{B/D}$. In particular, residues I780/Q784 of LBD$^{B/D}$ are involved in the interaction with CUB1 (Fig. 2e). On the basis of sequence and structure alignment (Extended Data Fig. 5), these critical interaction sites are fairly conserved in the amino acid sequence and in the 3D structure, except for ATD of GluK4 and GluK5 (ATD$^{GluK4/5}$). However, considering that NETO1 and NETO2 have different subunit-dependent regulation on GluK1 and GluK2 (refs. [12,21]), we speculate that these interactions determined in the GluK2–NETO2 complex might not fully reflect in different combinations of the GluK–NETO complex. Some changes of binding geometry or even new interactions might occur, which would profoundly alter regulatory effects of NETO proteins on KARs. In the GluK4 and GluK5 subtypes, R220 is substituted to a negatively charged Asp at the equivalent site (Extended Data Fig. 5a), which would repel negatively charged residues from NETO2 and thus prevent CUB1 from interacting with ATD$^{GluK4/5}$. Interestingly, GluK5 is shown to specifically occupy the B/D positions of the channel[15,17,22]; therefore, this unfavourable CUB1–ATD$^{GluK4/5}$ interaction would not prohibit NETO2 from associating with and modulating the heteromeric GluK2–GluK5 complex, which is a major population in the brain[23]. Nevertheless, we were unable to identify crucial residues of NETO2 involved in these GluK2–NETO2 interactions due to medium resolution of the NETO2 density.

To explore functional roles of these contacts, we substituted corresponding residues of GluK2 to Ala to disrupt the putative interactions with NETO2 (Extended Data Fig. 5a–d). The I780A/Q784A double mutation profoundly accelerated desensitization, probably due to the mutation destabilizing the LBD dimer. NETO2 is able to slow desensitization of GluK2$^{I780A/Q784A}$. The other mutations showed little effect on gating kinetics of GluK2 alone (Fig. 2f, Extended Data Fig. 6a). However, these mutations substantially decreased the effects of NETO2 on the GluK2 gating kinetics to different extents. In particular, NETO2 lost its function of regulating GluK2 upon introduction of the K216A/R220A mutations (GluK2$^{ATD\text{-}2A}$) (Fig. 2f), in line with a previous study that suggested that negatively charged residues of CUB1 have vital roles in modulation of NETO2 (ref. [24]). In addition, a triple point mutation (K448A/D450A/K451A) of GluK2 (GluK2$^{D1\text{-}3A}$) was designed to disturb contacts between CUB2 and D1-lobe$^{B/D}$. Compared with the wild-type GluK2–NETO2 complex, the GluK2$^{D1\text{-}3A}$–NETO2 complex displayed faster desensitization kinetics (Fig. 2f). Loop 1 of GluK2 was then substituted by the equivalent residues from GluK5 (GluK2$^{K5\text{-}loop1}$), and this mutant significantly reduced the effects of NETO2 on desensitization kinetics. However, an E723A/R727A double mutation in the D2-lobe (GluK2$^{D2\text{-}2A}$), which presumably disrupts the LDLa–D2-lobe interaction, showed a moderate decrease in slowing desensitization by NETO2 (Fig. 2f). NETO2 is able to attenuate inward rectification of the mutants discussed above (Extended Data Fig. 6b), suggesting that these mutations could not damage the association between GluK2 and NETO2.

Ion conduction pore of KARs

The LBD–TMD focused refinement yielded a 3.9 Å resolution map, which enabled us to build the most complete TMD model of the KAR so far (Fig. 3a, Extended Data Fig. 7). The pore profile reveals that the constriction sites are T652, A656 and T660 (Extended Data Fig. 7b), which is consistent with observations in previous studies[17,18]. Most importantly, the selectivity filter, consisting of the pore helix M2 (residues 608–620) and the pore loop (residues 621–625), was determined (Extended Data Fig. 7b). Residues on M2 helices form extensive hydrophobic interactions with M1 and M3 helices from the same subunit and M3 helices from adjacent subunits (Extended Data Fig. 7c). Furthermore, our construct has Q621 at the Q/R site located at the tip of the pore loop[25]. Its sidechain points upwards to the central vestibule (Extended Data Fig. 7b, d), and is aligned with residues at the Q/R site observed in AMPA receptor structures[26,27]. Previous investigations have shown that Arg at this site renders GluK2 calcium impermeable and attenuates polyamine block[28,29], presumably due to charge–charge repulsion. In addition, inside the selectivity filter, we determined a cation ligated by carbonyl oxygen groups from the four Q621 residues with bond lengths of 3.5–4 Å (Extended Data Fig. 7b, d). Given Gln is at the Q/R site, we propose that this cation is either a calcium or sodium ion.

Regulation of inward rectification

The long loops between M1 and M2 helices were resolved in the GluK2 map in the presence of NETO2. These loops extend into the cytosol and interact with each other, forming an intracellular cap domain (ICD) underneath the selectivity filter (Fig. 3b). Moreover, the amphiphilic H1 helix (residues 857–870) was built immediately after M4. The C terminus of H1 helix is positioned proximal to the C terminus of M1 and the M1–M2 loop from an adjacent subunit. Moreover, TM1^{NETO2} forms extensive hydrophobic interaction with TMD of GluK2. In particular, TM1^{NETO2} and its N-terminal α1 helix directly contact M1 of GluK2. One strip-like shape density was observed in between TM1^{NETO2} and M4 of GluK2, and is supposed to be the hydrophobic tail of a lipid molecule and important for bridging indirect contacts between TM1^{NETO2} and M4. On the intracellular side, the C terminus of TM1^{NETO2} competes with the H1 helix to interact with the C terminus of M1 and the N terminus of M2.

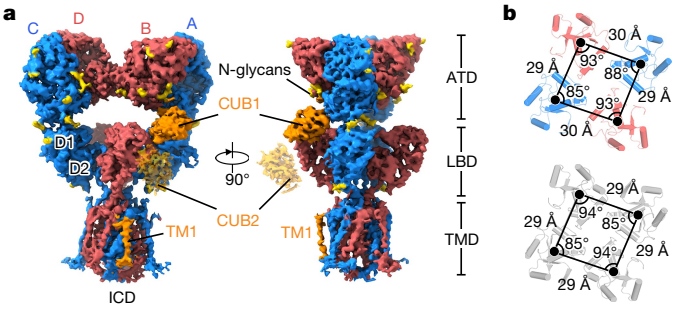

Fig. 4 | Architecture of the desensitized GluK2–NETO2 complex. a, The cryo-EM reconstruction of the GluK2-1×NETO2^{des} complex. Subunits A/C and B/D of the GluK2 complex are coloured in blue and red, respectively. The fragments of NETO2 are coloured in orange. The cryo-EM map of the CUB2 domain is extracted from the GluK2-1×NETO2^{des} map, shown at a lower threshold (yellow transparent) and overlaid on the same map of a higher threshold. **b**, Organization of the D2-lobe of the GluK2-1×NETO2^{des} complex (red and blue) and the desensitized GluK2 alone (grey). Centres of mass (COMs) of the lobes are depicted as black dots. Distances and angles are indicated.

To investigate the functional roles of the H1 helix and the ICD, we deleted the H1 helix (GluK2$^{\Delta H1}$) and substituted the M1–M2 linker with GluA2 equivalent residues (GluK2^{A2ICD}). We found that these mutations do not change receptor gating kinetics in the absence of NETO2. However, in the presence of NETO2, the GluK2$^{\Delta H1}$ and GluK2^{A2ICD} mutants showed slower and faster desensitization kinetics than wild-type GluK2, respectively (Fig. 3c). We speculate that these diametrically opposite effects on receptor desensitization kinetics result from a distinct ratio of the GluK2–NETO2 complex to the total receptors on the cell surface. Considering that the H1 helix blocks the NETO2-binding site but the ICD directly interacts with NETO2 (Fig. 3b), more GluK2$^{\Delta H1}$ would be fully occupied by NETO2 after deleting the H1 helix; by contrast, more NETO2 would dissociate from GluK2^{A2ICD} once the M1–M2 loop is changed to the equivalent loop from GluA2.

In regarding to inward rectification, the GluK2^{A2ICD} mutant is similar to wild-type GluA2, but distinct from wild-type GluK2, indicating that the M1–M2 loop has major roles in determining the inward rectification property of glutamate receptors. The M1–M2 loop of GluA2 was replaced by that from GluK2 (GluA2^{K2ICD}) and resulted in a substantial decrease of the GluA2 rectification (Fig. 3d, e, Extended Data Fig. 6c), further supporting that the M1–M2 loop is crucial for rectification. In the absence or presence of NETO2, the GluK2$^{\Delta H1}$ receptor shows comparable inward rectification as wild-type GluK2. We hypothesize that NETO2 competes with the H1 helix to stabilize the ICD of the receptor, creating a physical barrier that prohibits polyamine from diffusing close to the selectivity filter, thereby eliminating both polyamine inhibition and inward rectification.

Desensitized GluK2–NETO2 complex

We also obtained a 3.8 Å map of the desensitized GluK2–NETO2 complex (Fig. 4a, Extended Data Fig. 8, Extended Data Table 1), featuring GluK2 receptor binding with only one NETO2 subunit. The channel gate is closed, yet the LBD clamshell closure is nearly identical to the isolated LBD structure bound with kainate[30], indicating that the complex is stabilized at a desensitized state (GluK2-1×NETO2^{des}) (Extended Data Fig. 9a). Only CUB1 and TM1 of the NETO2 subunit are clearly visualized (Extended Data Fig. 9b). Consistent with desensitized KARs alone[18], the LBD layer of the GluK2-1×NETO2^{des} complex shows a disrupted LBD dimer and undergoes a remarkable rearrangement (Fig. 4a, b, Extended Data Fig. 9c, d). Structural comparison of LBD layers from the GluK2-1×NETO2^{des} complex and desensitized GluK2 alone shows that all of the four D2-lobes connecting to the gating helix M3 are superimposable, adopt a pseudo four-fold symmetry and are close to the channel central axis, suggesting that, in both the absence and the presence of NETO2, GluK2 receptors share similar mechanisms to decouple agonist binding from channel opening (Fig. 4b). The D1-lobes at B/D positions clearly show displacement between these two complexes. In the presence of NETO2, the D1-lobe of the B subunit approaches the ATD of the A subunit due to interactions with CUB1 of NETO2 (Extended Data Fig. 9e). In this desensitized state, the CUB2 and LDLa domains were not well determined (Fig. 4a, Extended Data Fig. 9c), suggesting that the interactions observed in the inhibited state were disrupted upon desensitization. Together, we speculate that, in the presence of NETO2, the inter-subunit connections of both ATD$^{A/C}$–LBD$^{B/D}$ and LBD$^{A/C}$–LBD$^{B/D}$, bridged by extracellular domains of NETO2, hinder rearrangement in the LBD layer upon desensitization, and thus slow down the desensitization kinetics. The ATD–CUB1 interaction is constitutively present in both inhibited and desensitized states. We hypothesize that the ATD–CUB1 interaction renders CUB1 an N-terminal anchor, whereas TM1 acts as a C-terminal anchor, constricting CUB2 and LDLa domains around the LBD layer during the gating cycle and thus modulating channel gating, underlying the essential role of the ATD–CUB1 interaction in the regulatory function of NETO2.

Online content

Any methods, additional references, Nature Research reporting summaries, source data, extended data, supplementary information, acknowledgements, peer review information; details of author contributions and competing interests; and statements of data and code availability are available at https://doi.org/10.1038/s41586-021-03936-y.

1. Herb, A. et al. The KA-2 subunit of excitatory amino acid receptors shows widespread expression in brain and forms ion channels with distantly related subunits. *Neuron* **8**, 775–785 (1992).
2. Bettler, B. et al. Cloning of a novel glutamate receptor subunit, GluR5: expression in the nervous system during development. *Neuron* **5**, 583–595 (1990).
3. Traynelis, S. F. et al. Glutamate receptor ion channels: structure, regulation, and function. *Pharmacol. Rev.* **62**, 405–496 (2010).
4. Castillo, P. E., Malenka, R. C. & Nicoll, R. A. Kainate receptors mediate a slow postsynaptic current in hippocampal CA3 neurons. *Nature* **388**, 182–186 (1997).
5. Vignes, M. & Collingridge, G. L. The synaptic activation of kainate receptors. *Nature* **388**, 179–182 (1997).
6. MacDermott, A. B., Role, L. W. & Siegelbaum, S. A. Presynaptic ionotropic receptors and the control of transmitter release. *Annu. Rev. Neurosci.* **22**, 443–485 (1999).
7. Chittajallu, R. et al. Regulation of glutamate release by presynaptic kainate receptors in the hippocampus. *Nature* **379**, 78–81 (1996).
8. Zhang, W. et al. A transmembrane accessory subunit that modulates kainate-type glutamate receptors. *Neuron* **61**, 385–396 (2009).
9. Copits, B. A., Robbins, J. S., Frausto, S. & Swanson, G. T. Synaptic targeting and functional modulation of GluK1 kainate receptors by the auxiliary neuropilin and tolloid-like (NETO) proteins. *J. Neurosci.* **31**, 7334–7340 (2011).
10. Tang, M. et al. Neto1 is an auxiliary subunit of native synaptic kainate receptors. *J. Neurosci.* **31**, 10009–10018 (2011).
11. Tomita, S. & Castillo, P. E. Neto1 and Neto2: auxiliary subunits that determine key properties of native kainate receptors. *J. Physiol.* **590**, 2217–2223 (2012).
12. Straub, C., Zhang, W. & Howe, J. R. Neto2 modulation of kainate receptors with different subunit compositions. *J. Neurosci.* **31**, 8078–8082 (2011).
13. Fisher, J. L. & Mott, D. D. The auxiliary subunits Neto1 and Neto2 reduce voltage-dependent inhibition of recombinant kainate receptors. *J. Neurosci.* **32**, 12928–12933 (2012).
14. Meyerson, J. R. et al. Structural mechanism of glutamate receptor activation and desensitization. *Nature* **514**, 328–334 (2014).
15. Mayer, M. L. Crystal structures of the GluR5 and GluR6 ligand binding cores: molecular mechanisms underlying kainate receptor selectivity. *Neuron* **45**, 539–552 (2005).
16. Kumari, J., Vinnakota, R. & Kumar, J. Structural and functional insights into GluK3–kainate receptor desensitization and recovery. *Sci. Rep.* **9**, 1–16 (2019).
17. Khanra, N., Brown, P. M., Perozzo, A. M., Bowie, D. & Meyerson, J. R. Architecture and structural dynamics of the heteromeric GluK2/K5 kainate receptor. *Elife* **10**, e66097 (2021).
18. Meyerson, J. R. et al. Structural basis of kainate subtype glutamate receptor desensitization. *Nature* **537**, 567–571 (2016).
19. Honore, T. et al. Quinoxalinediones: potent competitive non-NMDA glutamate receptor antagonists. *Science* **241**, 701–703 (1988).
20. Zhao, Y., Chen, S., Yoshioka, C., Baconguis, I. & Gouaux, E. Architecture of fully occupied GluA2 AMPA receptor–TARP complex elucidated by cryo-EM. *Nature* **536**, 108–111 (2016).

21. Copits, B. A. & Swanson, G. T. Dancing partners at the synapse: auxiliary subunits that shape kainate receptor function. *Nat. Rev. Neurosci.* **13**, 675–686 (2012).
22. Kumar, J., Schuck, P. & Mayer, M. L. Structure and assembly mechanism for heteromeric kainate receptors. *Neuron* **71**, 319–331 (2011).
23. Pinheiro, P. S. et al. Selective block of postsynaptic kainate receptors reveals their function at hippocampal mossy fiber synapses. *Cereb. Cortex* **23**, 323–331 (2013).
24. Li, Y.-J. et al. Neto proteins regulate gating of the kainate-type glutamate receptor GluK2 through two binding sites. *J. Biol. Chem.* **294**, 17889–17902 (2019).
25. Köhler, M., Burnashev, N., Sakmann, B. & Seeburg, P. H. Determinants of Ca^{2+} permeability in both TM1 and TM2 of high affinity kainate receptor channels: diversity by RNA editing. *Neuron* **10**, 491–500 (1993).
26. Chen, S. et al. Activation and desensitization mechanism of AMPA receptor–TARP complex by cryo-EM. *Cell* **170**, 1234–1246.e14 (2017).
27. Zhang, D., Watson, J. F., Matthews, P. M., Cais, O. & Greger, I. H. Gating and modulation of a hetero-octameric AMPA glutamate receptor. *Nature* **594**, 454–458 (2021).
28. Bowie, D. & Mayer, M. L. Inward rectification of both AMPA and kainate subtype glutamate receptors generated by polyamine-mediated ion channel block. *Neuron* **15**, 453–462 (1995).
29. Kamboj, S. K., Swanson, G. T. & Cull-Candy, S. G. Intracellular spermine confers rectification on rat calcium-permeable AMPA and kainate receptors. *J. Physiol.* **486**, 297–303 (1995).
30. Nayeem, N., Mayans, O. & Green, T. Correlating efficacy and desensitization with GluK2 ligand-binding domain movements. *Open Biol.* **3**, 130051 (2013).

Methods

Electrophysiology

Electrophysiological experiments were carried out using HEK 293T (Gibco; not authenticated; mycoplasma negative) cells, which were cultured in a 37 °C incubator supplied with 5% CO_2. cDNAs encoding GluK2 (UniProt ID: P42260) was subcloned into the vector pCAGGS-IRES-EGFP, and NETO2 (UniProt ID: C6K2K4) was subcloned into the vector pCAGGS-IRES-mCherry. Mutations in the gene encoding GluK2 was made by overlapping PCR and confirmed by Sanger sequencing. The total transfection system was 1 μg. When co-expression was carried out, the ratio between GluK2 and NETO2 was 1:1. The HEK 293T cells were transfected with lipofectomine2000 reagents (Invitrogen), expressed for 24–36 h and then dissociated with 0.05% trypsin. After resuspension, cells were placed on poly-D-lysine pretreated slides, and electrophysiological records were performed 4 h later.

Receptor desensitization was recorded on outside-out patches excised from the transfected HEK 293T cells. The external solution was (in mM): 140 NaCl, 2.5 KCl, 2 $CaCl_2$, 1 $MgCl_2$, 5 glucose and 10 HEPES (pH 7.4). Patch pipettes (resistance 3–5 MΩ) were filled with a solution containing (in mM): 130 KF, 33 KOH, 2 $MgCl_2$, 1 $CaCl_2$, 11 EGTA and 10 HEPES (pH 7.4). Glutamate (10 mM) diluted into the external solution was applied for 500 ms with a theta glass pipette mounted on a piezoelectric bimorph[25] every 12 s. Glutamate-induced currents were recorded with a holding potential of −70 mV and fitted with a double exponential function $A = A_0 \times (f_1 \exp(-t/\tau_f) + f_2 \exp(-t/\tau_s)) + C$. In these functions, t is the time. The currents amplitude (A) starts at A_0 and decays down to steady state C. f_1 and f_2 are the fractions of respective components as percentage ($f_1 + f_2 = 1$), and τ_f and τ_s are decay kinetics of fast and slow components. The weighted τ_{des} was calculated using the formula: weighted $\tau_{des} = f_1 \times \tau_f + f_2 \times \tau_s$.

The rectification of the receptors was analysed using whole-cell recordings on transfected HEK 293T cells. The extracellular solution was the same as that used in patch recording. The glass pipettes (3–5 MΩ) were filled with intracellular solution (in mM): 140 CsCl, 4 $MgCl_2$, 1 EGTA, 10 HEPES, 4 Na_2ATP and 0.1 spermine (pH 7.2). Desensitization curves (10 mM glutamate for 200 ms) were recorded while the holding potential was elevated from −100 with a step of 20 mV to +100 mV. The rectification index (RI) was calculated using the relative current amplitudes at +60 mV and −60 mV: $RI = (I_{+60\,mV} - I_{0\,mV})/(I_{0\,mV} - I_{-60\,mV})$. All the currents were collected with an Axoclamp 700B amplifier and Digidata 1440A (MolecularDevices), filtered at 2 kHz, and digitized at 10 kHz for whole-cell recordings and 100 kHz for outside-out patches. The current data were analysed using Clampfit software.

GluK2–NETO2 complex expression and purification

The full-length rat GluK2 cDNA sequence (UniProt ID: P42260) and rat NETO2 cDNA sequence (UniProt ID: C6K2K4) was cloned into the pEG BacMam vector[31]. Specifically, GluK2 and NETO2 were fused with a PreScission protease cleavage site (SNSLEVLFQ/GP), and a C-terminal mCherry-Twin strep tag and a GFP-His_8 tag, respectively. An incidental point mutation, F107L ($GluK2^{F107L}$), was introduced at the ATD layer during the cloning. The electrophysiological experiment indicates that $GluK2^{F107L}$ does not profoundly alter channel desensitization kinetics. Moreover, NETO2 exerts similar modulation on wild-type (WT) GluK2 and $GluK2^{F107K}$ in slowing down desensitization (Extended Data Fig. 1a–c). This variant was only used in the cryo-EM study, whereas the subsequent functional study was performed using WT GluK2. Subsequently, bicistronic bacmid and baculovirus harbouring the genes encoding GluK2 and NETO2 were generated and P2 viruses were used to infect suspension HEK 293F (Gibco; not authenticated; mycoplasma negative) cells at a cell density of approximately 2×10^6. Cell culture was infected with 10% (v/v) Gluk2–NETO2 baculoviruses to initiate transduction. Twelve hours after infection, 10 mM sodium butyrate and 20 μM 6,7-dinitroquinoxaline-2,3-dione (DNQX) were supplemented. Cells were harvested approximately 60 h post-infection and stored at −80 °C. We introduced the antagonist DNQX (20 μM) during the complex expression to reduce potential cell toxicity.

Cell pellets were resuspended in ice-cold buffer containing 20 mM HEPES (pH 7.5), 150 mM NaCl, 5 mM β-mercaptoethanol and protease inhibitors cocktail (Roche). The membrane was collected by ultracentrifugation at 4 °C (100,000*g* for 1 h). The GluK2–NETO2 complex was extracted with buffer containing 20 mM HEPES (pH 7.5), 150 mM NaCl, 5 mM β-mercaptoethanol, 20 μM DNQX and 1% (w/v) digitonin for 3 h at 4 °C. Insoluble material was removed by centrifugation (100,000*g* for 1 h). The supernatant was filtered and passed through Strep-Tactin Beads at 4 °C. The beads were washed with 20 mM HEPES (pH 7.5),150 mM NaCl, 5 mM β-mercaptoethanol, 20 μM DNQX and 0.08% (w/v) digitonin. Then, the GluK2–NETO2 complex was eluted with buffer containing 5 mM desthiobiotin. The fluorescent tags were cleaved by incubating with PreScission protease overnight at 4 °C. The GluK2–NETO2 complex was further purified by gel filtration chromatography (Superose-6, 10/300) with a buffer containing 20 mM HEPES (pH 7.5), 150 mM NaCl, 5 mM β-mercaptoethanol, 20 μM DNQX and 0.08% (w/v) digitonin. Peak fractions were pooled and concentrated to approximately 4.7 mg ml^{-1} for cryo-EM grids preparation. The fluorescence-detection size-exclusion chromatography (FSEC) experiment confirmed formation of the GluK2–NETO2 complex (Extended Data Fig. 1d–f).

Purification of the kainite-bound desensitized GluK2–NETO2 complex was carried out following the same procedure of the DNQX-bound inhibited complex without inhibitor supplemented during protein expression and purification. Agonist kainate was added to concentrated protein to achieve final concentrations of 5 mM immediately before cryo-EM grids preparation.

Cryo-EM sample preparation and data acquisition

Quantifoil R1.2/1.3 Cu 300 mesh grids were glow discharged for 60 s in H_2O_2 condition. Of the GluK2–NETO2 complex, 2.5 μl at 4.7 mg ml^{-1} was applied to the grid followed by blotting for 2.0 s at 100% humidity and 4 °C, and flash-frozen in liquid ethane using a Vitrobot Mark IV (Thermo Fisher Scientific).

Grids were imaged with a 300 kV Titan Krios (Thermo Fisher Scientific) or a 200 kV Talos Arctica (Thermo Fisher Scientific), both equipped with a K2 Summit direct electron detector (Gatan) and a GIF-Quantum energy filter. The slit width was set to 20 eV. A calibrated magnification of ×105,000 was used, yielded a pixel size of 1.36 Å or 1.32 Å on images (Extended Data Table 1). The defocus range was set to between −1.2 and −2.2 μm. All movie stacks were collected by SerialEM under a dose rate of 9.1–9.4 e^-/pixel/s with a total exposure time of 11.4 s, and dose-fractioned to 32 frames, resulting a total dose of 60 or 50 $e^-/Å^2$.

Single-particle cryo-EM data processing

For the DNQX-bound inhibited GluK2–NETO2 complex, a total of 5,448 movie stacks were collected, followed by motion correction using MotionCor2 (ref. [32]) with 5 × 5 patches. Parameters of the contrast transfer function (CTF) were estimated using Gctf[33], followed by particle picking using Gautomatch and Topaz[34]. Particles were classified into eight classes using a $GluK2_{EM}$ density map (EMDB ID: EMD-8289 (ref. [18])) as the reference map in RELION[35]. Three resulting maps (classes 6, 7 and 8) displayed classic KAR-like structural features, including the ATD, LBD and TMD. Moreover, one or two strings of globular densities were observed nearby GluK2. They appeared not to be an intrinsic part of GluK2 and were thus considered as soluble domains of NETO2. LBD densities in class 6 displayed an asymmetric organization, whereas their counterparts in classes 7 and 8 displayed a conventional dimer-of-dimers configuration. According to the different conformational states of LBD and stoichiometry of GluK2 and NETO2, the three classes were denoted as GluK2-1×$NETO2^{asymLBD}$ (class 6; 9.80%), GluK2-2×NETO2 (class 7; 5.09%) and GluK2-1×NETO2 (class 8; 6.42%),

respectively. Particles were then imported to cryoSPARC for processing[36]. Non-uniform refinement gave rise to initial maps at 4.3 Å, 7.1 Å and 5.1 Å, respectively. Two rounds of ab initio reconstruction were subsequently conducted to remove junk particles, followed by another round of heterologous refinement using low-passed maps as references, at 7, 15 and 30 Å, respectively. The final round of non-uniform refinement generated 4.1 Å, 6.4 Å and 4.2 Å full-length reconstructions according to the golden-standard Fourier shell correlation (GSFSC) criterion[37], illustrating hallmark features of glycosylation sites, LBD clamshells and transmembrane helices. The LBD–TMD map of the GluK2-2×NETO2 complex is significantly improved by LBD–TMD focused refinement in the presence of C2 symmetry, generating a 5.6 Å map with more continuous transmembrane helices.

To improve the resolution of the LBD–TMD of the GluK2-1×NETO2 complex, focused classification and refinement were conducted. Masks were created using a GluK2-1×NETO2 map whose ATDs were manually erased. Masked 3D classification in RELION generated three classes[35]. Among them, only class 1 (28.2%) displayed continuous and clear transmembrane densities. The final map of LBD–TMD was generated by non-uniform refinement in cryoSPARC with a LBD–TMD mask, which was reported at 3.9 Å according to the GSFSC criterion[37]. GluK2 LBD and TMD were well resolved in this new map with abundant features, including sidechain density for most aromatic residues, visible loops between LBD and TMD, and intact structures of both the SF and pore loop, which allowed us to build the TMD of GluK2. The linker between M2 and M3 became visible and aided us to trace the backbone of this linker. This map also reveals two N-glycans inside linkers between the LBD and TMD layer, and these glycosylation sites facilitate sequence registration for S1–pre-M1 and S2–M4 linkers during model building.

For the kainate-bound desensitized GluK2-1×NETO2 complex, a total of 2,957 movie stacks were collected, followed by motion correction using MotionCor2, CTF estimation using Gctf, and particle picking using Gautomatch and Template Picker (cryoSPARC). The initial 3D classification without imposition of mask or symmetry generated eight classes, four of which displayed KAR-like structural features but with poor NETO2 density and were subjected to a second round of 3D classification in RELION, yielding three classes. Class 1 showed a density connecting ATD–LBD and clearly represent the GluK2–NETO2 complex. One round of ab initio reconstruction and two rounds of heterologous refinement were then carried out in cryoSPARC to further clean up particles. The map quality was substantially improved. The final map was generated using non-uniform refinement, and the structure was determined at 3.8 Å according to the GSFSC criterion[37].

Model building

Model building of the LBD–TMD part of GluK2 started with the 3.9 Å LBD–TMD map, containing receptor LBD–TMD and NETO2 CUB1–LDLa–TM1. The map clearly showed densities for most of the aromatic residues and N-glycans, which allowed us to reliable build the model. The D1 lobe (residues 431–535 and 762–806), D2 lobe (residues 536–544 and 669–761) and TMD (residues 545–668 and 806–850) were extracted from the structure of *Rattus norvegicus* GluK2 (PDB ID: 5KUF[18]). The homology models of CUB2 and LDLa were prepared using the SWISS-MODEL utility based on homology structures with PDB IDs of 2WNO and 6H03, respectively[38,39]. All of these domains were fitted into the cryo-EM map as rigid bodies using UCSF Chimera software. The resulting model was then manually inspected and adjusted in COOT[40], followed by refinement against the cryo-EM map in real space using the phenix.real_space_refine utility[41].

The model of CUB1 of NETO2 was generated using SWISS-MODEL based on a homology model (PDB ID: 2QQL)[42]. The ATD layer of GluK2 was extracted from a crystal structure of GluK2 (PDB ID: 5KUF[18]). Subsequently, the homology models of ATD and LBD–TMD of GluK2, CUB1 and CUB2–LDLa–TM1 of NETO2 were docked into cryo-EM maps of the GluK2-1×NETO2, GluK2-2×NETO2 and GluK2-1×NETO2^{asymLBD} complex as rigid bodies, generating corresponding complex structures. The resulting models were subsequently manually inspected and adjusted in COOT. Given the medium resolution of the maps of overall structure, the models of rigid body were refined against the cryo-EM map in real space using phenix.real_space_refine.

For the GluK2-1×NETO2^{des} complex, the ATD layer, D1 lobe, D2 lobe, TMD and CUB1 were extracted from the structure of GluK2-1×NETO2, which were docked into the cryo-EM map as rigid bodies using UCSF Chimera software. The resulting model was then manually inspected and adjusted in COOT, followed by refinement against the cryo-EM map in real space using phenix.real_space_refine. The model stereochemistry was evaluated using the comprehensive validation (cryo-EM) utility in the PHENIX software package.

All figures were prepared with ChimeraX or PyMOL (Schrödinger, LLC)[43,44].

Reporting summary

Further information on research design is available in the Nature Research Reporting Summary linked to this paper.

Data availability

The 3D cryo-EM density maps of the antagonist DNQX-bound GluK2-1×NETO2, LBD–TMD of the GluK2-1×NETO2, GluK2-2×NETO2, GluK2-1×NETO2^{asymLBD} complex and the agonist kainate-bound desensitized GluK2-1×NETO2^{des} complex have been deposited in the Electron Microscopy Database under the accession codes EMD-31462, EMD-31464, EMD-31463, EMD-31459 and EMD-31460, respectively. The cryo-EM map of LBD–TMD of the GluK2-2×NETO2 complexes have been deposited as an additional map under entry EMD-31463. The coordinates for the structures have been deposited in the PDB under accession codes 7F59, 7F5B, 7F5A, 7F56 and 7F57, respectively. Source data are provided with this paper.

31. Goehring, A. et al. Screening and large-scale expression of membrane proteins in mammalian cells for structural studies. *Nat. Protoc.* **9**, 2574–2585 (2014).
32. Zheng, S. Q. et al. MotionCor2: anisotropic correction of beam-induced motion for improved cryo-electron microscopy. *Nat. Methods* **14**, 331–332 (2017).
33. Zhang, K. Gctf: real-time CTF determination and correction. *J. Struct. Biol.* **193**, 1–12 (2016).
34. Bepler, T., Kelley, K., Noble, A. J. & Berger, B. Topaz-Denoise: general deep denoising models for cryoEM and cryoET. *Nat. Commun.* **11**, 5208 (2020).
35. Zivanov, J. et al. New tools for automated high-resolution cryo-EM structure determination in RELION-3. *Elife* **7**, e42166 (2018).
36. Punjani, A., Rubinstein, J. L., Fleet, D. J. & Brubaker, M. A. cryoSPARC: algorithms for rapid unsupervised cryo-EM structure determination. *Nat. Methods* **14**, 290–296 (2017).
37. Scheres, S. H. & Chen, S. Prevention of overfitting in cryo-EM structure determination. *Nat. Methods* **9**, 853–854 (2012).
38. Bordoli, L. et al. Protein structure homology modeling using SWISS-MODEL workspace. *Nat. Protoc.* **4**, 1–13 (2009).
39. Briggs, D. C. et al. Metal ion-dependent heavy chain transfer activity of TSG-6 mediates assembly of the cumulus-oocyte matrix. *J. Biol. Chem.* **290**, 28708–28723 (2015).
40. Emsley, P. & Cowtan, K. Coot: model-building tools for molecular graphics. *Acta Crystallogr. D Biol. Crystallogr.* **60**, 2126–2132 (2004).
41. Afonine, P. V. et al. Real-space refinement in PHENIX for cryo-EM and crystallography. *Acta Crystallogr. D Struct. Biol.* **74**, 531–544 (2018).
42. Appleton, B. A. et al. Structural studies of neuropilin/antibody complexes provide insights into semaphorin and VEGF binding. *EMBO J.* **26**, 4902–4912 (2007).
43. Goddard, T. D. et al. UCSF ChimeraX: meeting modern challenges in visualization and analysis. *Protein Sci.* **27**, 14–25 (2018).
44. DeLano, W. L. Pymol: an open-source molecular graphics tool. *CCP4 Newsletter on Protein Crystallography* http://148.79.162.84/newsletters/newsletter40/11_pymol.html (2002).

Acknowledgements We thank X. Huang, B. Zhu, X. Li, L. Chen and other staff members at the Center for Biological Imaging (CBI), Core Facilities for Protein Science at the Institute of Biophysics, Chinese Academy of Science (IBP, CAS) for the support in cryo-EM data collection; N. Sheng for providing the cDNAs of GluK2 and NETO2; and Y. Wu for his research assistant service. This work is funded by the Chinese Academy of Sciences Strategic Priority Research Program (grant XDB37030304 to Y.Z. and grant XDB37030301 to X.C.Z.), the National Key R & D Program of China (2019YFA0801603 to Y.S.S.), the National Natural Science Foundation of China (91849112 to Y.S.S. and 31971134 to X.C.Z.), the Natural Science Foundation of Jiangsu

Province (BE2019707 to Y.S.S.) and the Fundamental Research Funds for the Central Universities (0903-14380029 to Y.S.S.).

Author contributions Y.Z. conceived the project and supervised the research. L.H., J.S., W.A. and B.Y. carried out molecular cloning and the cell biology experiments. L.H. expressed and purified the protein complex sample. L.H., Y.D. and Y.W. prepared the sample for the cryo-EM study. Y. Gao. L.H., Y.W. and Y.D. carried out cryo-EM data collection. Y. Gao and Y.Z. processed the cryo-EM data and prepared the figures. B.L. and H.L. built and refined the atomic model. Y.Z. and X.C.Z. analysed the structure. Y.Z. and Y.S.S. designed the electrophysiological study. J.S. and Y. Ge performed the electrophysiological analysis. Y.Z. prepared the initial draft of the manuscript. X.C.Z., Y.S.S. and Y.Z. edited the manuscript with input from all authors in the final version.

Competing interests The authors declare no competing interests.

Additional information

Supplementary information The online version contains supplementary material available at https://doi.org/10.1038/s41586-021-03936-y.

Correspondence and requests for materials should be addressed to Xuejun Cai Zhang, Yun Stone Shi or Yan Zhao.

Peer review information *Nature* thanks Ingo Greger and Geoffrey Swanson for their contribution to the peer review of this work. Peer reviewer reports are available.

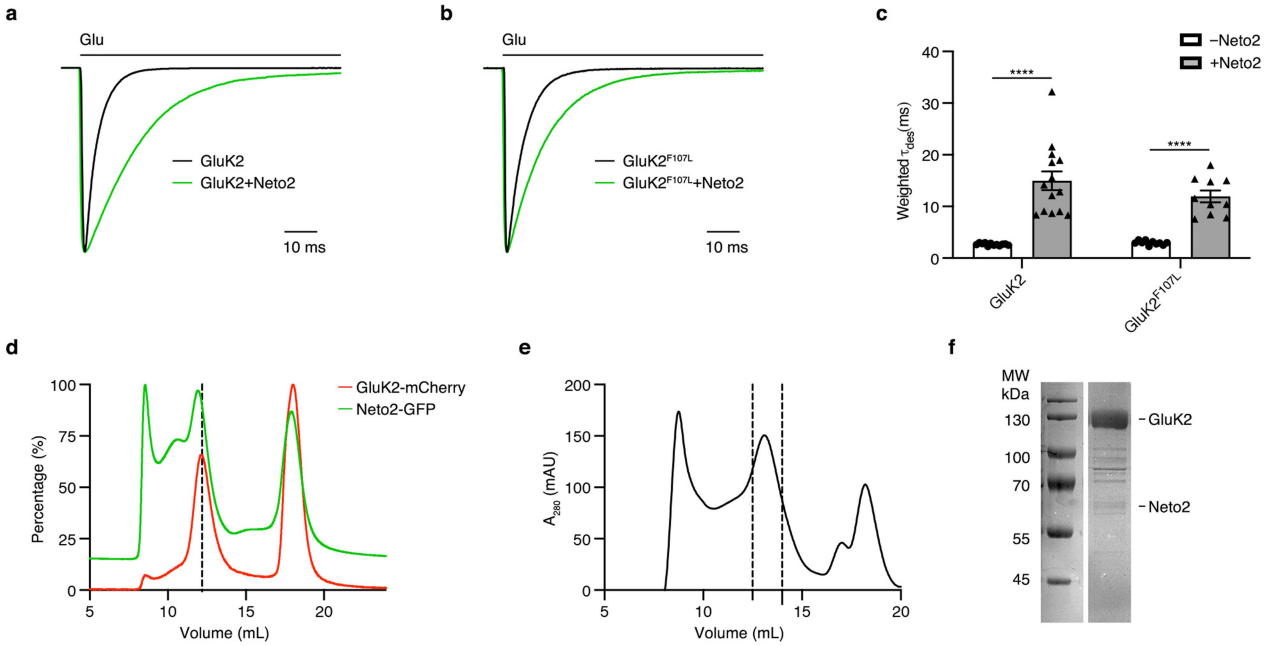

Extended Data Fig. 1 | Functional study and purification of GluK2-Neto2 complex. a, **b**, Outside-out recording of the WT GluK2 and GluK2^{F107L}, in the absence or presence of Neto2. **c**, Statistical analysis of the desensitization time constant of the WT GluK2 and GluK2^{F107L}, with or without Neto2 (GluK2, $n = 12$, GluK2 + Neto2, $n = 14$; GluK2^{F107L}, $n = 10$; GluK2^{F107L} + Neto2, $n = 10$). Each symbol represents a single cell recording, and n value represents biologically independent cells for statistical analysis. Significances were determined using two-sided unpaired t-test. ****, $P < 0.0001$. Similar results were reproduced from two independent experiments. Error bars stand for S.E.M. **d**, Fluorescence-detection size-exclusion chromatography (FSEC) analysis of the co-expressed GluK2-mCherry (red) and Neto2-GFP (green). The experiments were repeated independently with more than three times with similar results. **e**, Size-exclusion chromatography (SEC) profile of the purified GluK2-Neto2 complex. Fractions within the dashed lines were pooled for cryo-EM sample preparation. The experiments were repeated independently with more than three times with similar results. (**f**) Coomassie blue-stained SDS-PAGE gel of the pooled fractions. The gel was repeated three times from different batches of purification with similar results. The uncropped gel can be found in Supplementary Fig. 1.

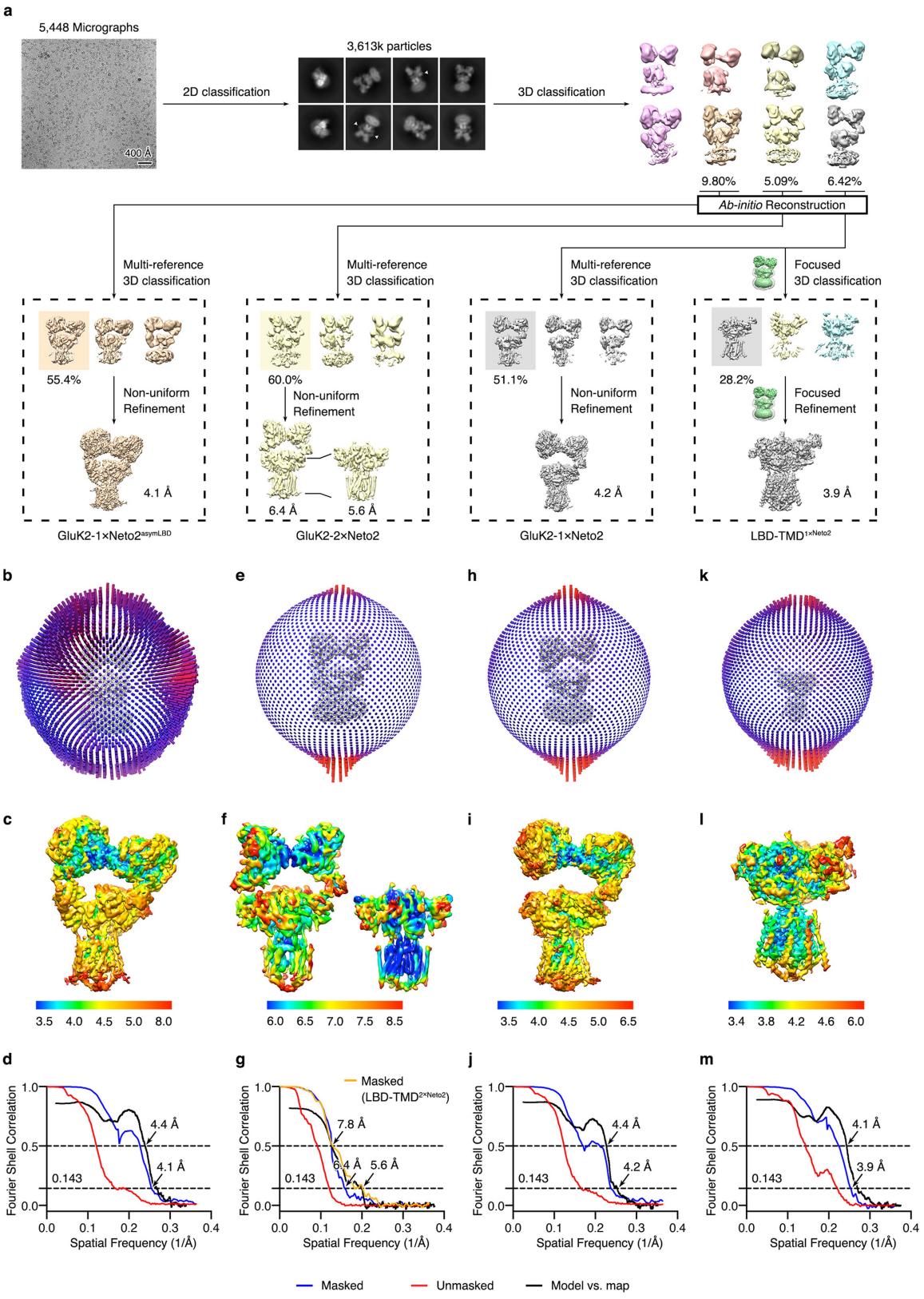

Extended Data Fig. 2 | See next page for caption.

Extended Data Fig. 2 | Cryo-EM data analysis of GluK2-1×Neto2, GluK2-2×Neto2, and GluK2-1×Neto2^{asymLBD} complex. a, Flowchart of cryo-EM data processing. A total of 5,448 movie stacks were collected and motion-corrected, followed by CTF estimation and particle picking. A representative motion-corrected micrograph of this dataset is shown here (Scale bar = 40 nm). The experiments were repeated three times with similar results. Particles were cleaned and classified using several rounds of 2D and 3D classifications, which generated 3 classes, representing GluK2-1×Neto2, GluK2-2×Neto2, and GluK2-1×Neto2^{asymLBD}, respectively. Particles were then submitted to further 3D classifications separately to improve resolutions. Focused classification and refinement of LBD-TMD were conducted on the particles of GluK2-1×Neto2 complex. Masks used in focused processing were overlaid on GluK2 map (green) as transparent grey surfaces alongside the arrows. **b**, **e**, **h**, **k**, Angular distribution of the particles contributing the final reconstruction for GluK2-1×Neto2^{asymLBD} complex (**b**), GluK2-2×Neto2 complex (**e**), GluK2-1×Neto2 complex (**h**), and LBD-TMD (**k**). The length of each spike indicates of the number of particles in the designated orientation. **c**, **f**, **i**, **l**, Sharpened map of GluK2-1×Neto2^{asymLBD} complex (**c**), GluK2-2×Neto2 complex (**f**), GluK2-1×Neto2 complex (**i**), and LBD-TMD (**l**), colored according to local resolution estimation. **d**, **g**, **j**, **m**, The half-map (red) and model-map (black) Fourier shell correlation (FSC) of GluK2-1×Neto2^{asymLBD} complex (**d**), GluK2-2×Neto2 complex (**g**), GluK2-1×Neto2 complex (**j**), and LBD-TMD (**m**).

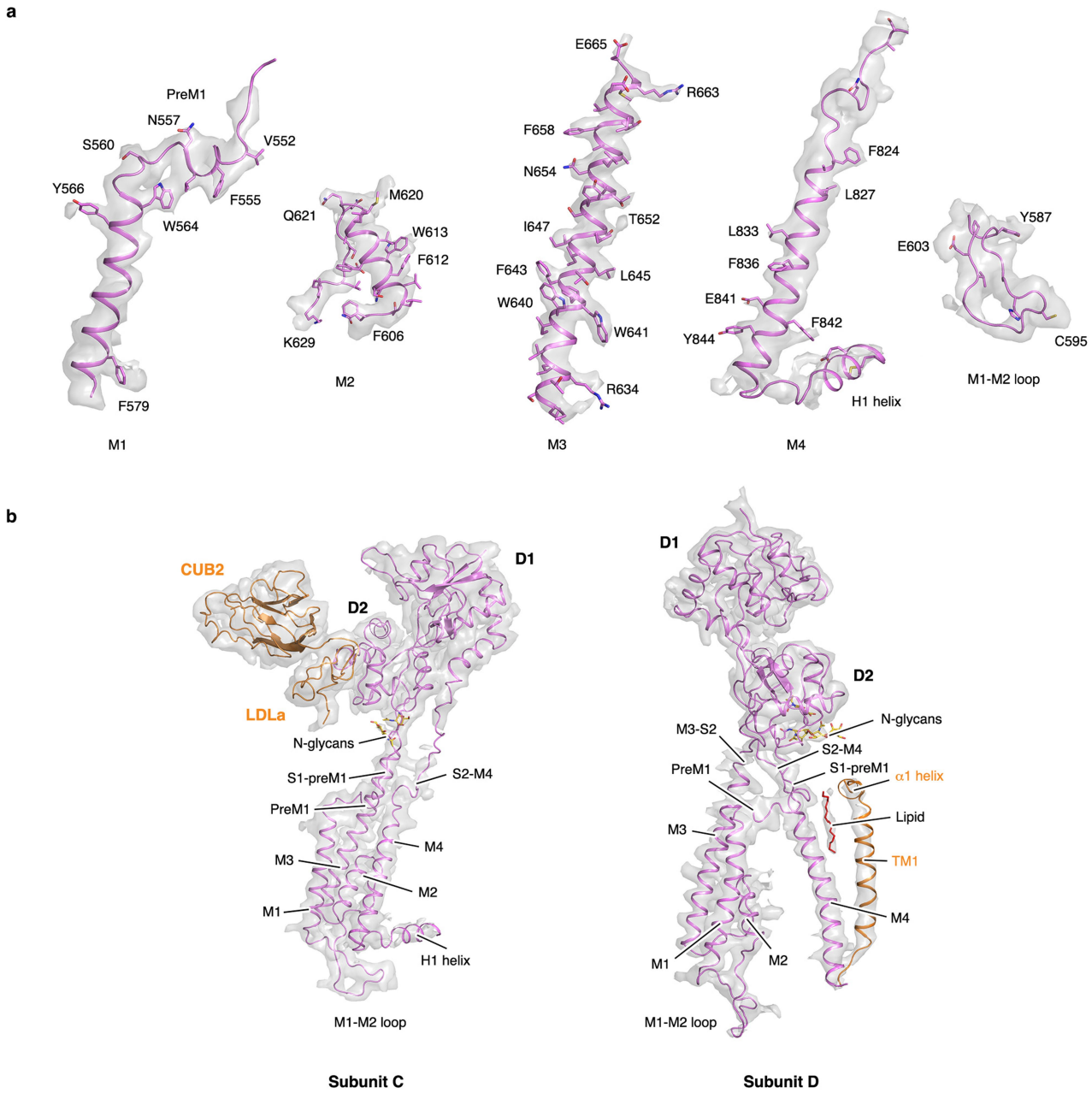

Extended Data Fig. 3 | EM maps for transmembrane helices and the LBD-TMD. a, Transmembrane helices M1–M4, and the M1-M2 loop. EM maps are shown as transparent grey surfaces. Some sidechains are shown as sticks. **b**, EM maps for LBD and TMD layers. CUB2 and LDLa of Neto2 are colored in orange. Receptor is colored in purple. N-glycans and a lipid tail are shown in sticks.

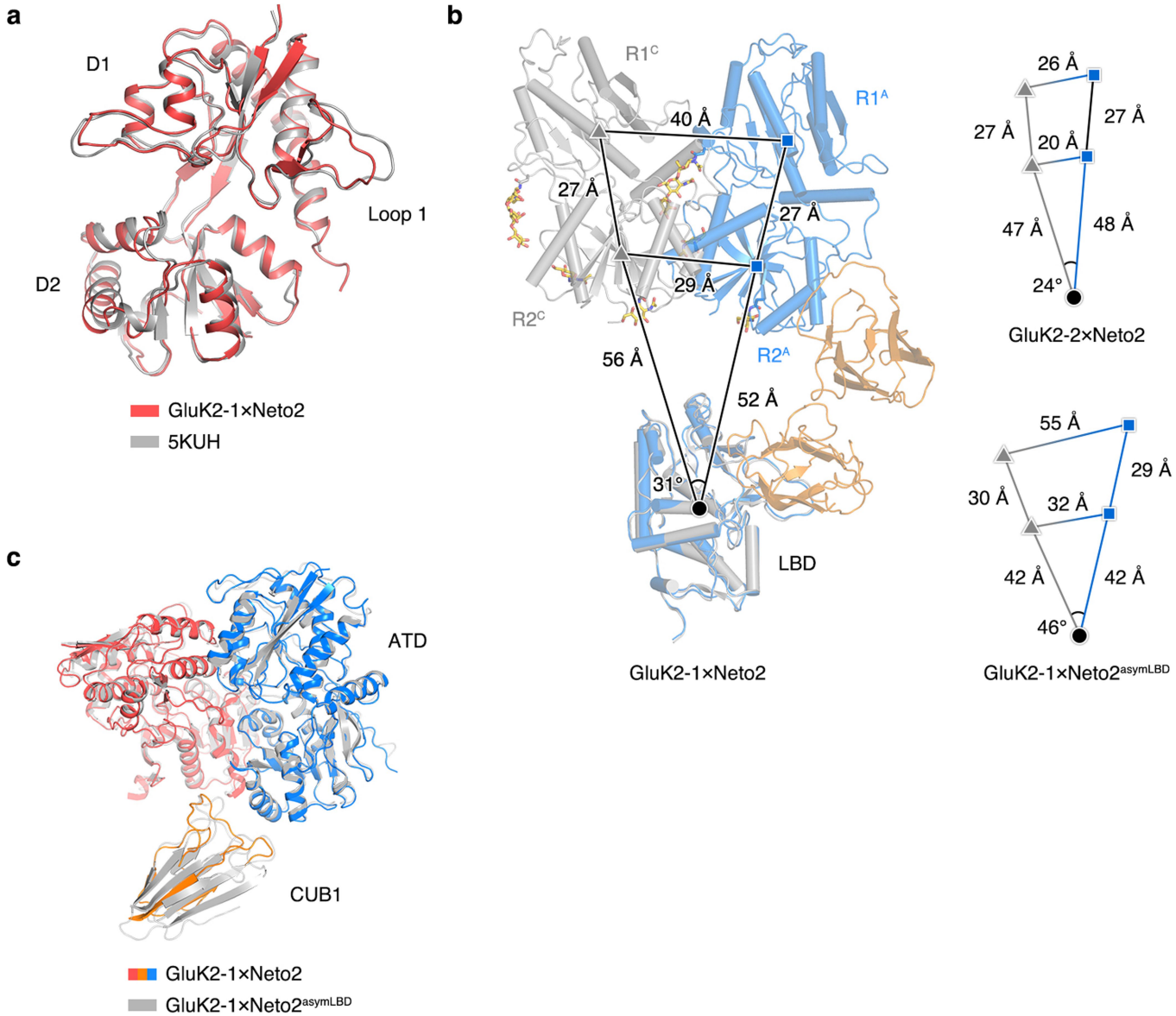

Extended Data Fig. 4 | Structural comparison of ATD and LBD layers. **a**, Superimposition of antagonist bound LBDs of 5KUH (grey) and GluK2-1×Neto2 (red). **b**, Comparison of the ATD^{A}-LBD^{B} and ATD^{C}-LBD^{D} segments between subunit A (grey) and C (blue) of the GluK2-1×Neto2, GluK2-2×Neto2 and GluK2-1×Neto2^{asymLBD} complexes, using LBD as a reference. The COMs of the ATD R1/R2-lobe of subunits A and C are depicted as rectangles or triangles, respectively. The COMs of the LBD layer is marked as a circle. **c**, Superimposition of ATD-CUB1 interactions between GluK2-1×Neto2^{asymLBD} (grey) and GluK2-1×Neto2 (red, orange and blue).

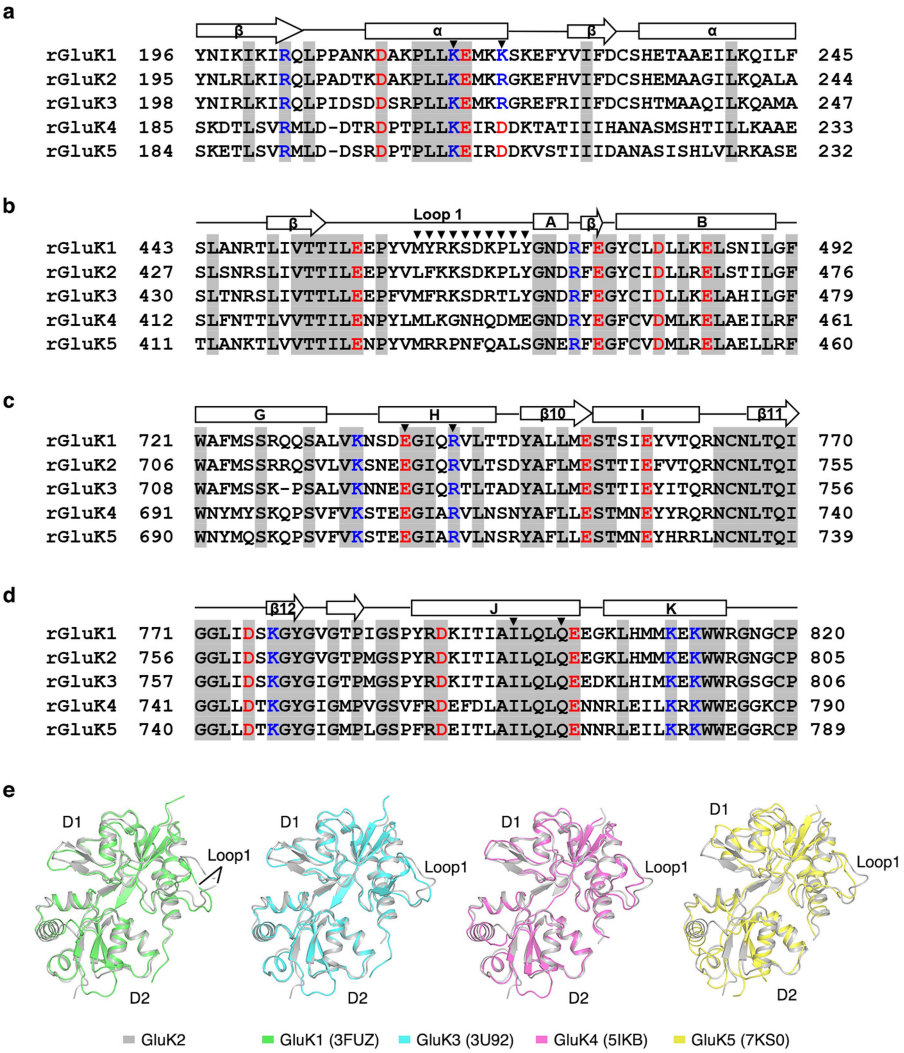

Extended Data Fig. 5 | Sequence alignments and structural comparison of the KARs. a–**d**, Sequence alignments of the GluK members in *Rat norvegicus*, numbered according to full-length subunits. Secondary structures of GluK2 are marked above the sequence alignment. Dashes represent gaps. Conserved residues are shaded in grey. Residues which are involved in Neto2 interaction are indicated by triangle symbol. **e**, Structural comparison of the LBD of GluK2 with GluK1 (3FUZ, green), GluK3 (3U92, cyan), GluK4 (5IKB, magenta), and GluK5 (7KS0, yellow), respectively. D1- and D2- lobes and Loop 1 are indicated.

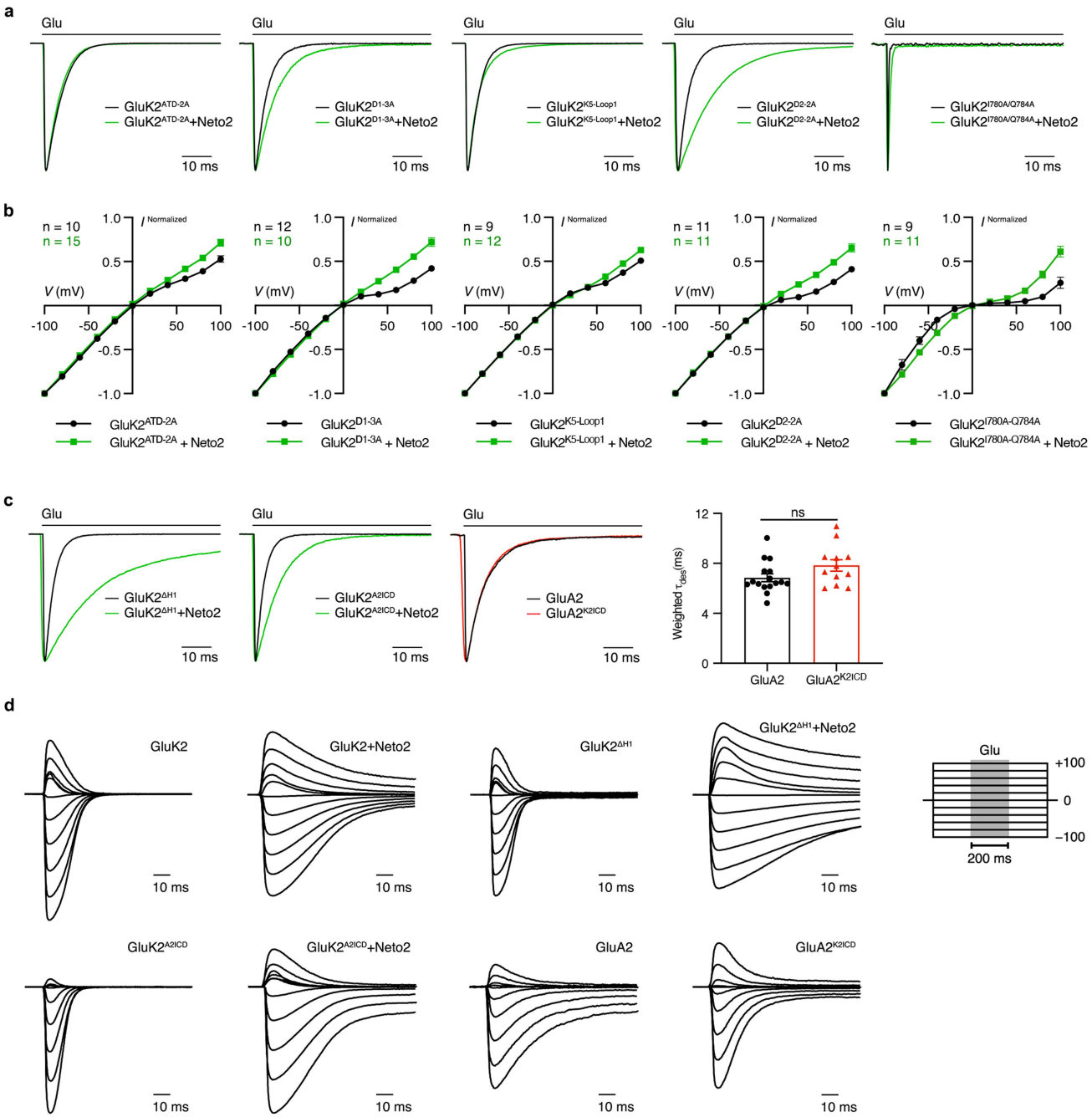

Extended Data Fig. 6 | Representative desensitization and rectification traces. a, Representative desensitization traces of GluK2 and mutants responded to 60 ms application of 10 mM glutamate were normalized and aligned to the peak. Superimposed responses of the receptor alone and the receptor-Neto2 complex were shown in black and green traces, respectively. **b**, Normalized current-voltage relationship of GluK2 mutants in the absence and presence of Neto2. *n* value represents independent cells for analysis. **c**, Representative desensitization traces and related statistical analysis (GluA2, $n = 16$; $GluA2^{K2ICD}$, $n = 12$). Each symbol represents a single cell recording, and *n* value represents biologically independent cells for statistical analysis. Significances were determined using two-sided unpaired t-test. Not significant (ns), P = 0.0755. No adjustments were made for multiple comparisons. Error bars stand for S.E.M. The H1-helix is composed of residues ^{857}FCSAMVEELRMSLK^{870} and removed in $GluK2^{\Delta H1}$ construct. The amino acid sequence of the ICD of GluK2 and GluA2 between M1-M2 helices are ^{587}YEWYNPHPCNPDSDVVEN^{604} and ^{570}YEWHTEEFEDGRETQSSESTNE^{591}, respectively, which are involved in the ICD swapping constructs of $GluA2^{K2ICD}$ and $GluK2^{A2ICD}$. **d**, I-V relationship for GluA2, GluK2 and related mutants. Desensitization curves (10 mM glutamate for 200 ms) were recorded at holding potential ranging from −100 to +100 mV in 20 mV increasement. Traces were normalized to the peak value at −100 mV.

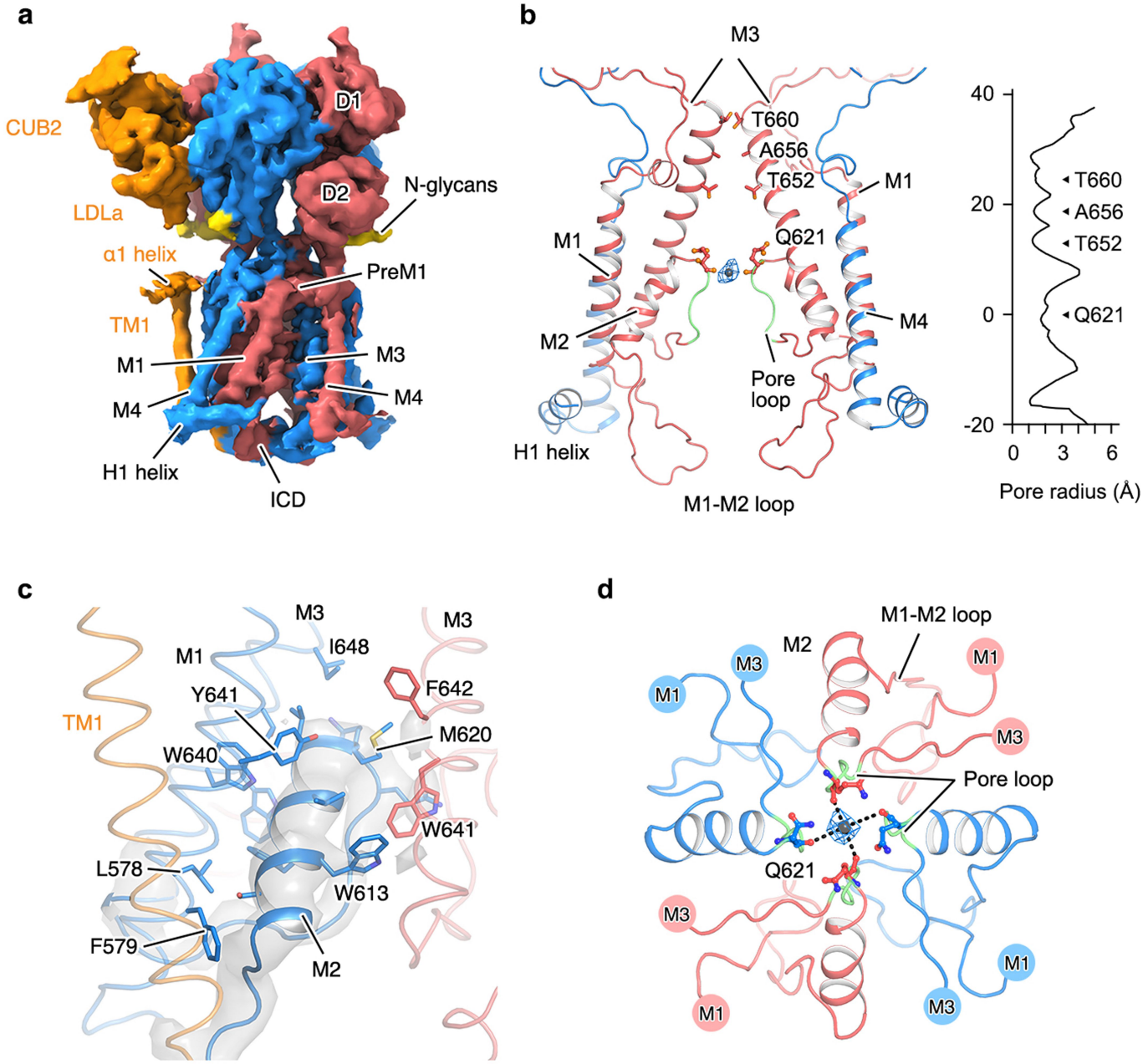

Extended Data Fig. 7 | Interactions stabilizing the pore helix M2. a, EM density map of the LBD and TMD layers of the GluK2-1×Neto2 complex. Subunits A/C and B/D of GluK2 are colored in blue and red, respectively. The Neto2 protein is colored in orange. N-glycans are colored in yellow. **b**, The ion conduction pore and its profile of the GluK2-Neto2 complex. Pore loops are colored in green. A cation ion is shown as a grey sphere, overlaid with corresponding EM density colored in marine. Q621, T652, A656, and T660 are shown in sticks. Constriction sites are indicated in the pore profile. **c**, The TM helices of the GluK2 (red and blue) and the Neto2 (yellow) are shown as cartoon. The EM density of M2 helix are shown as transparent grey surface. Critical residues involved in interactions are shown as sticks. **d**, "Top-down" view of M2 helices and the pore loops. Q621 residues are shown in sticks.

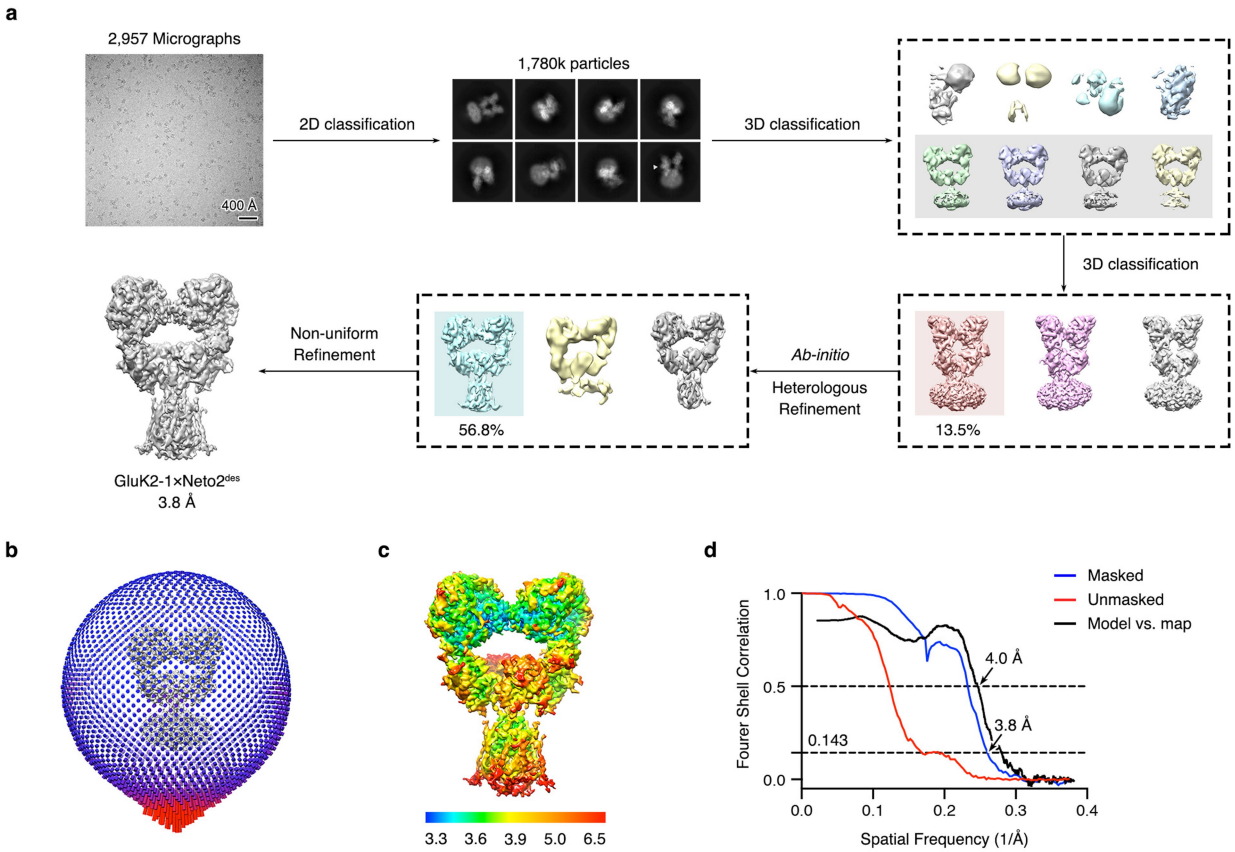

Extended Data Fig. 8 | Cryo-EM data analysis of GluK2-1×Neto2^{des} complex. **a**, Flowchart of cryo-EM data processing. A total of 2,957 movie stacks were collected and motion-corrected, followed by CTF estimation and particle picking. A representative motion-corrected micrograph of this dataset is shown here (Scale bar = 40 nm). The experiments were repeated three times with similar results. Three-dimensional classification generated 8 classes, 4 of which displayed classical structures of kainate receptors. Another round of 3D classification was then performed, followed by *Ab-initio* Reconstruction and Heterologous Refinement to furtherly improve the quality of map. **b**, Angular distribution of the particles contributing the final reconstruction of GluK2-1×Neto2^{des} complex. The length of each spike indicates of the number of particles in the designated orientation. **c**, Sharpened map of GluK2-1×Neto2^{des} complex, colored according to local resolution estimation. **d**, The half-map (red) and model-map (black) Fourier shell correlation.

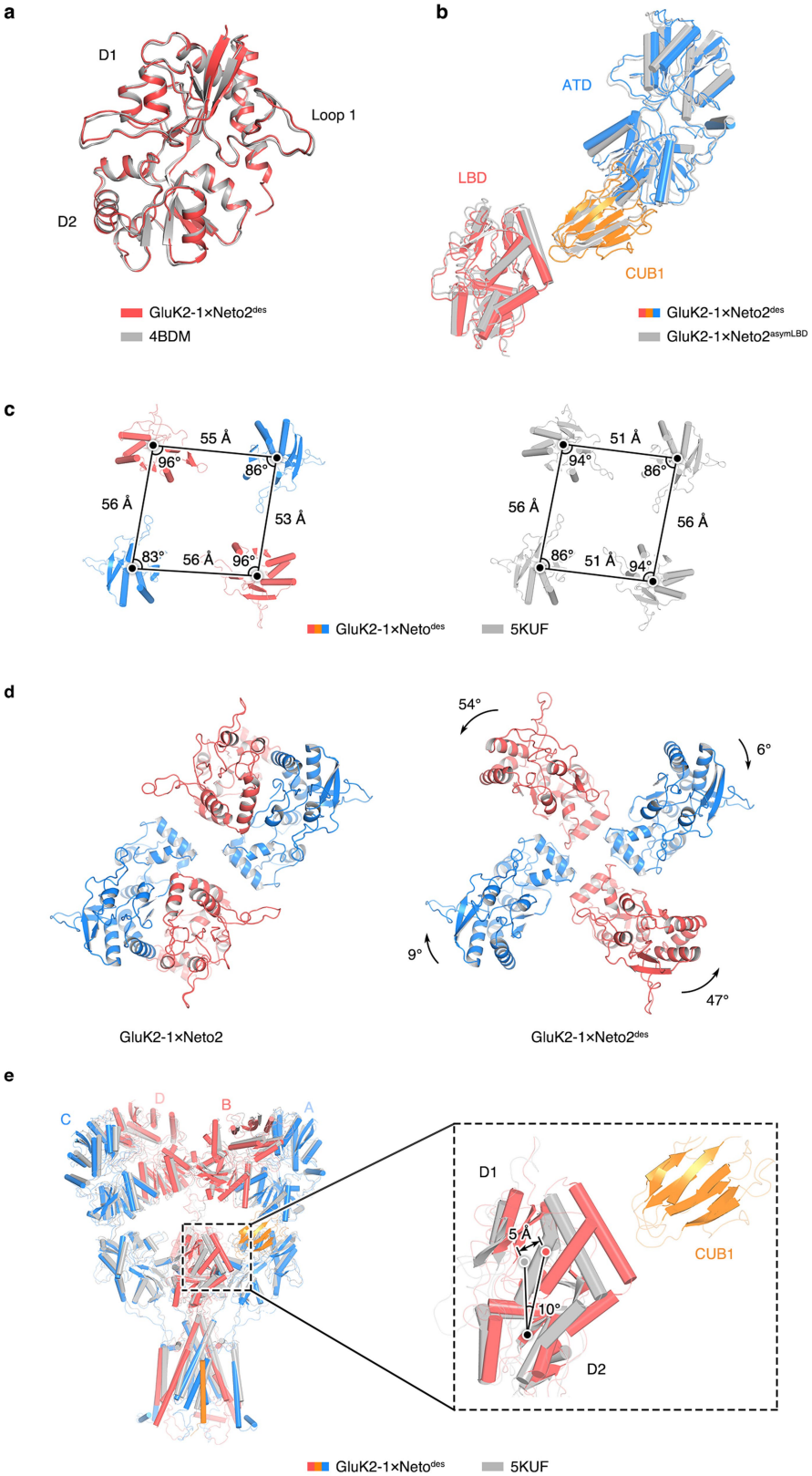

Extended Data Fig. 9 | Conformational change of GluK2-Neto2 complex upon desensitization. a, Superimposition of agonist bound LBDs of 4BDM (grey) and GluK2-1×Neto2^{des} (red). **b**, Superimposition of ATD-CUB1-LBD interactions between GluK2-1×Neto2^{asymLBD} (grey) and GluK2-1×Neto2^{des} (red, orange and blue). **c**, Organization of the D1 lobe of the GluK2-1×Neto2^{des} (red and blue) and desensitized GluK2 alone (grey). COMs of the lobes are depicted as black dots. Distances and angles are indicated. **d**, The LBD rearrangement between GluK2-1×Neto2 and GluK2-1×Neto2^{des} upon desensitization. **e**, Displacement of LBD at B-position of GluK2-1×Neto2^{des} complex (red, blue and orange) compared with desensitized GluK2 (5KUF, grey).

Extended Data Table 1 | Cryo-EM data collection, refinement and validation statistics

	GluK2-1×Neto2 (EMDB-31462) (PDB 7F59)	GluK2-2×Neto2 (EMDB-31463) (PDB 7F5A)	GluK2-1×Neto2^{asymLBD} (EMDB-31459) (PDB 7F56)	LBD-TMD$^{1×Neto2}$ (EMDB-31464) (PDB 7F5B)	GluK2-1×Neto2^{des} (EMDB-31460) (PDB 7F57)
Data collection and processing					
Magnification	105,000 ×	105,000 ×	105,000 ×	105,000 ×	105,000 ×
Voltage (kV)	300	300	300	300	200
Electron exposure (e^{-}/Å^2)	60	60	60	60	50
Defocus range (μm)	–1.2 ~ –2.2	–1.2 ~ –2.2	–1.2 ~ –2.2	–1.2 ~ –2.2	–1.2 ~ –2.2
Pixel size (Å)	1.36	1.36	1.36	1.36	1.32
Symmetry imposed	C1	C1	C1	C1	C1
Initial particle images (no.)	3,613,377	3,613,377	3,613,377	3,613,377	1,780,151
Final particle images (no.)	248,423	45,644	90,580	148,300	92,785
Map resolution (Å)	4.2	6.4	4.1	3.9	3.8
FSC threshold	0.143	0.143	0.143	0.143	0.143
Map resolution range (Å)	3.5 ~ 6.5	6.0 ~ 8.5	3.5 ~ 8.0	3.4 ~ 6.0	3.3 ~ 6.5
Refinement					
Initial model used (PDB code)	5KUF	5KUF	5KUF	5KUF	5KUF
Model resolution (Å)	4.4	7.8	4.4	4.1	4.0
FSC threshold	0.5	0.5	0.5	0.5	0.5
Map sharpening *B* factor (Å^2)	–153	–400	–111	–200	–103
Model composition					
Non-hydrogen atoms	28,968	31,274	27,825	15,360	27,860
Protein residues	3,628	3,925	3,468	1,921	3,468
Ligands	20	22	27	14	29
B factors (Å^2)					
Protein	385.84	305.39	109.72	250.69	412.69
Ligands	130.55	117.62	30.00	220.07	260.83
R.m.s. deviations					
Bond lengths (Å)	0.008	0.008	0.008	0.011	0.007
Bond angles (°)	1.067	1.220	1.105	1.604	0.967
Validation					
MolProbity score	2.53	2.40	2.52	2.61	2.23
Clashscore	28.36	23.53	26.96	27.07	16.77
Poor rotamers (%)	0.13	0.56	1.10	0.6	0.56
Ramachandran plot					
Favored (%)	88.49	90.57	89.38	83.29	91.52
Allowed (%)	11.51	9.43	10.62	16.71	8.48
Disallowed (%)	0.00	0.00	0.00	0.00	0.00

Statistical analysis of cryo-EM data processing and model validation of GluK2-1×Neto2, GluK2-2×Neto2, and GluK2-1×Neto2^{asymLBD}, LBD-TMD$^{1×Neto2}$ and GluK2-1×Neto2^{des}, prepared using PHENIX software package.

nature research

Corresponding author(s): Yan Zhao, Yun Stone Shi, Xuejun Cai Zhang

Last updated by author(s): Jul 30, 2021

Reporting Summary

Nature Research wishes to improve the reproducibility of the work that we publish. This form provides structure for consistency and transparency in reporting. For further information on Nature Research policies, see our Editorial Policies and the Editorial Policy Checklist.

Statistics

For all statistical analyses, confirm that the following items are present in the figure legend, table legend, main text, or Methods section.

n/a	Confirmed	
☐	☒	The exact sample size (*n*) for each experimental group/condition, given as a discrete number and unit of measurement
☐	☒	A statement on whether measurements were taken from distinct samples or whether the same sample was measured repeatedly
☐	☒	The statistical test(s) used AND whether they are one- or two-sided *Only common tests should be described solely by name; describe more complex techniques in the Methods section.*
☒	☐	A description of all covariates tested
☐	☒	A description of any assumptions or corrections, such as tests of normality and adjustment for multiple comparisons
☐	☒	A full description of the statistical parameters including central tendency (e.g. means) or other basic estimates (e.g. regression coefficient) AND variation (e.g. standard deviation) or associated estimates of uncertainty (e.g. confidence intervals)
☐	☒	For null hypothesis testing, the test statistic (e.g. *F*, *t*, *r*) with confidence intervals, effect sizes, degrees of freedom and *P* value noted *Give P values as exact values whenever suitable.*
☒	☐	For Bayesian analysis, information on the choice of priors and Markov chain Monte Carlo settings
☒	☐	For hierarchical and complex designs, identification of the appropriate level for tests and full reporting of outcomes
☒	☐	Estimates of effect sizes (e.g. Cohen's *d*, Pearson's *r*), indicating how they were calculated

Our web collection on statistics for biologists contains articles on many of the points above.

Software and code

Policy information about availability of computer code

Data collection	SerialEM 3.8 was used for cryo-EM image collection; Clampfit 10.4.0.36 was used for electrophysiological data collection.
Data analysis	MotionCor 2 1.3.2, GCTF 1.06, Gautomatch 0.56, Topaz 0.2.4, cryoSPARC 3.0, RELION 3.1, PyMOL 3.2, UCSF ChimeraX 1.11, COOT 0.9.2-pre, PHENIX 1.16

For manuscripts utilizing custom algorithms or software that are central to the research but not yet described in published literature, software must be made available to editors and reviewers. We strongly encourage code deposition in a community repository (e.g. GitHub). See the Nature Research guidelines for submitting code & software for further information.

Data

Policy information about availability of data

All manuscripts must include a data availability statement. This statement should provide the following information, where applicable:

- Accession codes, unique identifiers, or web links for publicly available datasets
- A list of figures that have associated raw data
- A description of any restrictions on data availability

The sequences of rat GluK2 and Neto2 are available in the following links:
GluK2 (UniProt ID: P42260): https://www.uniprot.org/uniprot/P42260
Neto2 (UniProt ID: C6K2K4): https://www.uniprot.org/uniprot/C6K2K4

The novel structures determined in this study are deposited in PDB Bank and Electron Microscopy Data Bank (EMDB):
GluK2-1xNeto2: 7F59; EMD-31462
GluK2-2xNeto2: 7F5A; EMD-31463

GluK2-1xNeto2asymLBD: 7F56; EMD-31459
GluK2-1xNeto2des: 7F57; EMD-31460
LBD-TMD1xNeto2: 7F5B; EMD-31464

Field-specific reporting

Please select the one below that is the best fit for your research. If you are not sure, read the appropriate sections before making your selection.

☒ Life sciences ☐ Behavioural & social sciences ☐ Ecological, evolutionary & environmental sciences

For a reference copy of the document with all sections, see nature.com/documents/nr-reporting-summary-flat.pdf

Life sciences study design

All studies must disclose on these points even when the disclosure is negative.

Sample size	Sample sizes were not predetermined for this study. For the cryo-EM studies, the number of micrographs is determined by the available microscope time. For the electrophysiology experiments, the authors have recorded 10 or more cells/patches for each constructs, which are sufficient enough to see real effects of the mutations based on the reproducibility of the results. The sample sizes of all these experiments were determined based on the consistency and variability.
Data exclusions	No data was excluded from the analyses.
Replication	Sample preparation related experiments including purification and SDS-PAGE gel electrophoresis were reproduced at least three times independently. Whole cell patch clamp recording were reproduced with about 10 different cells. All attempts at replication were successful.
Randomization	For cryo-EM studies, meshes on the cryo-EM grids were randomly selected for data collection. Division of datasets into two random halves was done based on standard approach in RELION 3.1. For electrophysiology experiments, randomization is not relevant as no group allocations were performed.
Blinding	The investigators were not blinded as the parameters for cryo-EM analysis and electrophysiology experiments did not require subjective assessments of the treatments or their outcomes that might otherwise influence the validity of the results.

Reporting for specific materials, systems and methods

We require information from authors about some types of materials, experimental systems and methods used in many studies. Here, indicate whether each material, system or method listed is relevant to your study. If you are not sure if a list item applies to your research, read the appropriate section before selecting a response.

Materials & experimental systems

n/a	Involved in the study
☒	☐ Antibodies
☐	☒ Eukaryotic cell lines
☒	☐ Palaeontology and archaeology
☒	☐ Animals and other organisms
☒	☐ Human research participants
☒	☐ Clinical data
☒	☐ Dual use research of concern

Methods

n/a	Involved in the study
☒	☐ ChIP-seq
☒	☐ Flow cytometry
☒	☐ MRI-based neuroimaging

Eukaryotic cell lines

Policy information about cell lines

Cell line source(s)	FreeStyle 293-F cells (Gibco, USA); 293-T cells (Gibco, USA)
Authentication	Not authenticated.
Mycoplasma contamination	The cells were tested negative for mycoplasma contamination.
Commonly misidentified lines (See ICLAC register)	Not commonly misidentified lines were used.